

Graphene-Antenna Sandwich Photodetector

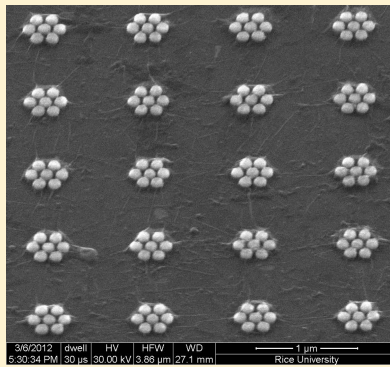
Zheyu Fang,^{*,†,||,⊥} Zheng Liu,^{§,⊥} Yumin Wang,^{†,⊥} Pulickel M. Ajayan,[§] Peter Nordlander,^{†,‡} and Naomi J. Halas^{*,†,‡}

[†]Department of Electrical and Computer Engineering, Laboratory for Nanophotonics, [‡]Department of Physics and Astronomy, and [§]Mechanical Engineering and Materials Science Department, Rice University, Houston, Texas 77005, United States

^{||}School of Physics, State Key Lab for Mesoscopic Physics, Peking University, Beijing 100871, China

 Supporting Information

ABSTRACT: Nanoscale antennas sandwiched between two graphene monolayers yield a photodetector that efficiently converts visible and near-infrared photons into electrons with an 800% enhancement of the photocurrent relative to the antennaless graphene device. The antenna contributes to the photocurrent in two ways: by the transfer of hot electrons generated in the antenna structure upon plasmon decay, as well as by direct plasmon-enhanced excitation of intrinsic graphene electrons due to the antenna near field. This results in a graphene-based photodetector achieving up to 20% internal quantum efficiency in the visible and near-infrared regions of the spectrum. This device can serve as a model for merging the light-harvesting characteristics of optical frequency antennas with the highly attractive transport properties of graphene in new optoelectronic devices.



KEYWORDS: Plasmonics, graphene, Fano resonances, hot electron, field enhancement

Graphene is a material of great promise for new electronic devices due to its unusually high electron mobility, atomic layer thickness, and unique mechanical flexibility.^{1–4} Its broadband absorption makes graphene a tantalizing candidate for solar cells, ultrafast photodetectors, and terahertz modulators.^{5–7} The nonlocal carrier-assisted intrinsic photoresponse in dual-gated graphene p–n junction devices has been investigated;^{8–10} however, the inherently low absorption cross section and quantum efficiency of graphene seriously limit its usefulness for high-performance photonic or optoelectronic devices.¹¹ In contrast, optical frequency antennas have been shown to be highly efficient harvesters of visible and near-infrared light at wavelengths chosen by tailoring the size and shape of the antenna structure. Surface plasmons, the collective electron oscillations supported by metals, provide the dominant mechanism for the antenna response in this wavelength range. Nanoscale optical frequency antennas have been exploited in a wide range of applications in subwavelength optics, surface-enhanced spectroscopies, and sensing.^{12–20} It has recently been shown that noble metal films and nanoparticles can modify the properties of graphene in devices through their characteristic surface plasmons.^{21,22} Although electrically doped graphene, as a semimetal, also possesses plasmonic properties attractive for active material applications,^{23,24} this property is not available at visible and near-infrared spectral wavelengths. These complementary properties suggest that marrying optical frequency antenna structures with graphene-based devices may provide opportunities to enhance and extend the properties of graphene toward light-based applications in the visible regime.

Plasmonic clusters^{25,26} are ideal candidate structures for merging the properties of nanoscale antennas with those of graphene. Plasmonic cluster geometries exhibit tunable Fano resonances, consisting of a transparency window where scattering is strongly suppressed and hot electron–hole pair generation is the dominant absorption mechanism. As a consequence, the near field associated with the transparency window is strongly enhanced.²⁷ When incident light is resonant with this transmission window, the intense near field will be capable of efficiently enhancing the direct excitation (DE) of electron–hole pairs in a single-atom-thick graphene layer (0.3 nm), provided it is in direct proximity of the high-intensity near field region of the cluster. Additionally, since graphene possesses no bandgap, hot electrons (HE) created in the gold structure^{28,29} can transfer directly into the conduction band of the graphene sheet.³⁰ Because of the high mobility of graphene, both sources of photon-induced graphene conduction electrons, DE and HE, can flow directly into the electrical circuit and be detected as a photocurrent.

In this Letter, we report the fabrication and characterization of a tightly integrated plasmonic antenna–graphene photodetector consisting of Fano-resonant plasmonic clusters sandwiched between two single-atom-thick layers of graphene in a planar device (Figure 1A). Source–drain electrodes and plasmonic patterns were first fabricated on a graphene substrate

Received: May 10, 2012

Revised: June 14, 2012

Published: June 15, 2012



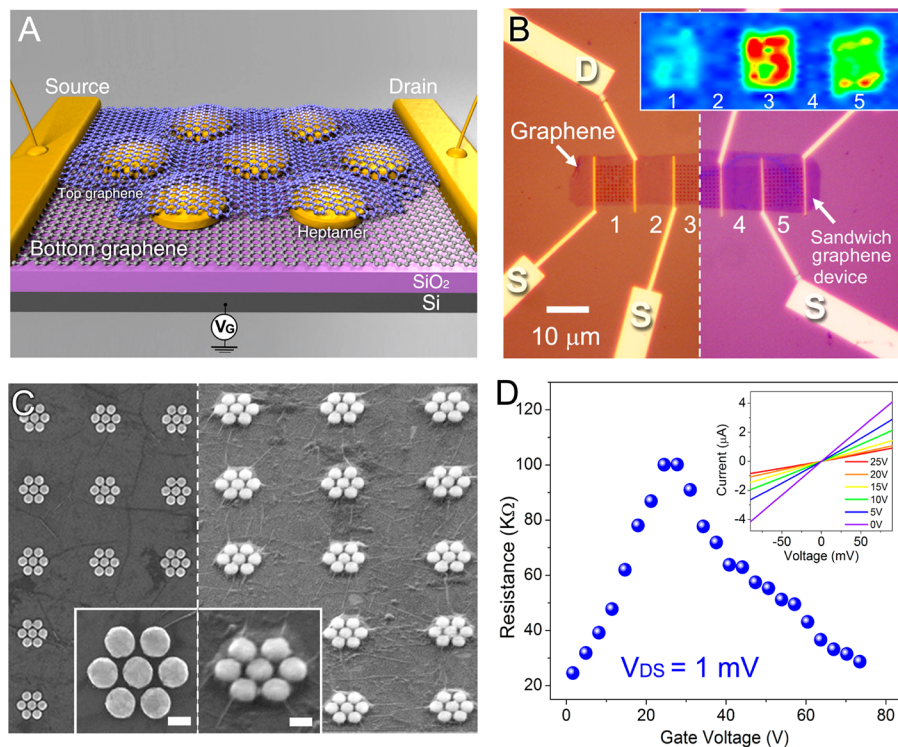


Figure 1. Graphene–antenna sandwich photodetector. (A) Schematic illustration of a single gold heptamer sandwiched between two monolayer graphene sheets. V_G is the gate voltage used to electrostatically dope the graphene. (B) Optical microscopy image of the as-fabricated device before (left) and after (right) deposition of the second graphene layer. Inset: Raman mapping (G mode) of device areas 1–5 under 785 nm excitation. (C) SEM image of heptamer array fabricated in area 3, as indicated in (B). (D) Electrical transport characteristic at a drain bias of 1 mV. Inset: I – V plots for various gate voltages V_G from 0 to 25 V.

by two-step E-beam lithography and subsequent lift-off (Figure 1B, left side). The structure was then covered by a second graphene layer to form a sandwich device³¹ (Figure 1B and Supporting Information Figure S1 and S2). In the device shown in Figure 1B, plasmonic antennas (dimers, heptamers, and nonamers) were fabricated in areas 1, 3, and 5, respectively, while areas 2 and 4 were left antenna free. The graphene sheet placed atop the heptamers is clearly observed in the scanning electron microscope (SEM) image of the device structure (Figure 1C right, inset). Because of its flexibility, the top graphene sheet conforms to the plasmonic cluster profile, relaxing around it and into the gaps between the component gold discs of the structure (Supporting Information Figure S3). The plasmonic cluster component disks are all 130 nm in diameter, and the interparticle gap distance is 15 nm, large enough to easily accommodate the conforming graphene sheet. The scale bar of the inset (higher SEM magnification) is 100 nm.

Raman imaging reveals the spatial and spectral regions of strongest antenna–graphene coupling in the device (Figure 1B, inset). With 514 nm laser illumination, there is almost no variation in Raman intensity across the device since this is wavelength is nonresonant with the device antennas. For 785 nm laser illumination, however, significant enhancements of the graphene Raman modes can be observed in regions 3 and 5 of the device, since this wavelength is resonant with the Fano resonances of the heptamer and nonamer antennas (Supporting Information Figure S4). The field-effect transistor measurements were performed using a four-probe station at a vacuum of $\sim 10^{-5}$ Torr. The dependence of resistance on gate voltage observed indicates that the Dirac point (band-crossing energy)

is reached at a gate voltage of $V_G \sim 30$ V (Figure 1D). The applied source–drain voltage is 1 mV. The inset consists of linear I – V characteristics obtained at gate biases ranging from 0 to 25 V. The device mobility is estimated to be $\mu = [dI_{DS}/dV_G] \times [L/(WC_iV_{DS})]$,³² where L is the channel length (~ 50 \$\mu\text{m}), W is the channel width (~ 10 \$\mu\text{m}), and C_i is the real capacitance per unit area between the channel and the back-gate ($\sim 1.2 \times 10^{-8}$ F/cm²). The estimated mobilities range from 350 to 1300 cm² V⁻¹ s⁻¹.

When measuring the local photocurrent in the device by performing a line scan of the excitation laser (785 nm wavelength, 1 \$\mu\text{m}\$ beam spot) between the source and drain electrodes, an antisymmetric photocurrent response is observed (Figure 2A). The distance between the edge plasmonic structures and the contacts is 1 \$\mu\text{m}\$, and we recorded photocurrent for each 0.5 \$\mu\text{m}\$ step as the spot was scanned across the device. For each measurement, the illumination antenna area was equivalent. The inset shows a schematic of the line scan path and the zero current point. The photocurrent obtained from these devices is directly determined by the geometry of the patterned dimer and heptamer structures with their Fano resonance tuned to the incident laser at 785 nm. The antenna-patterned regions enhance the photocurrent significantly compared to the unpatterned regions of the device. For the case of dimer antennas, the photocurrent can be made to be dependent upon the polarization of the incident laser (Figure 2B). A $\cos^2 \theta$ angular dependence characteristic of a dimer antenna characterizes this highly polarization-dependent response.

For incident light at the Fano resonance wavelength of the heptamer antennas, the photocurrent of the corresponding

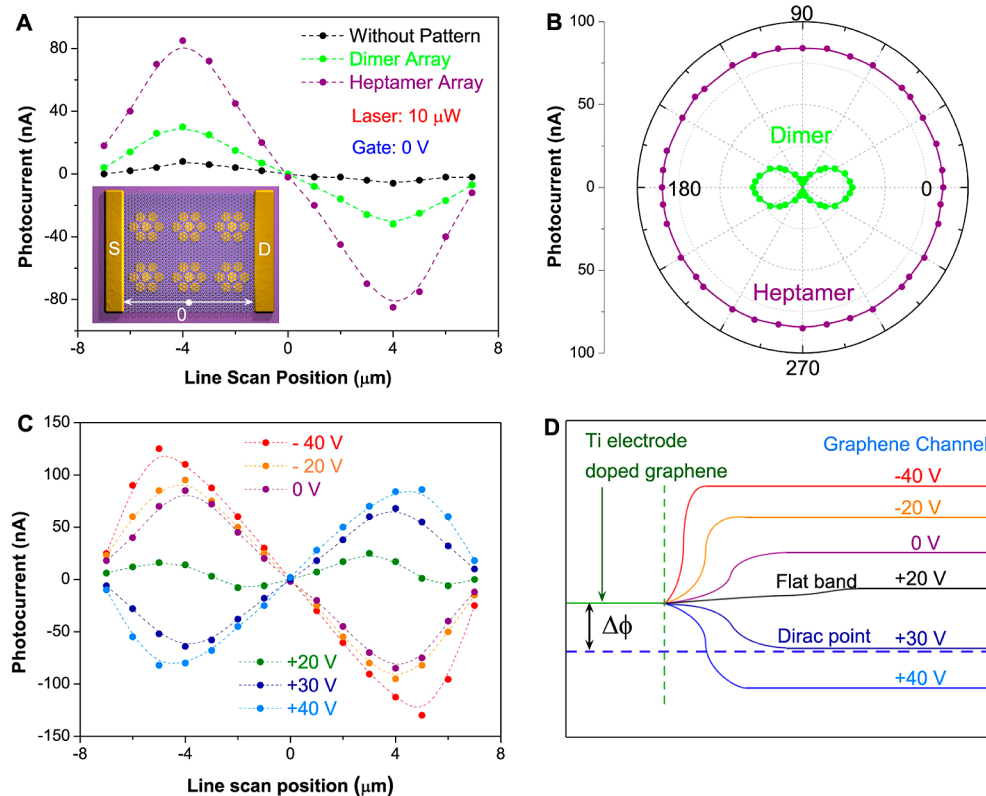


Figure 2. Photocurrent characterization of antenna–graphene sandwich devices. (A) Photocurrent measurements show antisymmetric photocurrent responses from the different regions of the device corresponding to specific plasmonic antenna geometries, obtained along the line scan direction. The zero point is indicated in the inset schematic. The black dots indicate the photocurrent detected without the plasmonic antennas present in the device. (B) Polarization dependence of the photocurrent of the dimer antennas in region 1 of the device (green dots) and the heptamer antennas in region 3 of the device (purple dots). (C) Measured photocurrent for gate bias V_G between -40 to $+40$ V for the heptamer antenna-patterned region 3 of the device, the incident laser power of $10 \mu\text{W}$. (D) Schematic of the surface potentials inferred from the photocurrent line scans at each gate bias.,

device region is almost three times larger than that of the dimer region of the device, and eight times larger than the pristine graphene regions of the device. The variation in responsivity for the different antenna geometries is due to their contrasting scattering and absorption characteristics. Compared with the dimer, the heptamer has a much larger absorption cross section, which provides larger field enhancements, multiple hot spots, and a greater yield of hot electrons. An even larger photocurrent can be achieved for the nonamer antennas in region 5 of the device (Supporting Information Figure S5). This is because the nonamer has a much deeper Fano minimum (close to 100%) compared to the heptamer, providing significantly larger near field enhancement which results in an increased yield of DE carriers in the graphene layers.

To further realize active device tuning and switching, a gate bias was applied to shift the Fermi level of the graphene. The measured photocurrents for the bare graphene and heptamer patterned graphene device region for V_G varying from -40 to $+40$ V (Figure 2C, and Table S1 of Supporting Information) show the same characteristic: the photocurrent goes to zero when the laser focus is moved to the center of the graphene channel. For a larger negative gate bias, the maximum photocurrent appears at a position closer to the source and drain electrodes, and a larger photocurrent response is measured. When the gate bias is positive, almost no photocurrent is observed. Further increasing the gate voltage

changes the direction and increases the magnitude of the photocurrent.

These characteristics are directly related to the local variations in the bandfilling of graphene for different gate voltages (Figure 2D). Because of symmetry, only half of the band structure needs to be shown. The blue dashed line indicates the graphene Fermi level, while the solid line represents the Dirac point of graphene. The Ti contact dopes the graphene, because its work function (4.33 eV) is lower than that of graphene (4.5 eV).³³ Therefore, the Fermi level in the area of the electrodes will be raised slightly toward the Dirac point. The energy difference $\Delta\phi$ between the Fermi level and the doped graphene band is a Schottky barrier, independent of bias. The bias thus only tunes the Fermi level of the graphene channel in the middle of each region of the device. The plasmonic structures were fabricated onto the graphene without a Ti adhesion layer, so they would not introduce impurities or dopants into the graphene device.

For zero gate voltage, the difference of Fermi levels between doped graphene and the graphene channel leads to band bending in the region extending from the electrodes (Figure 2D). An internal electric field is generated, which separates the electron–hole pairs excited by incident light, resulting in a photocurrent. The current reaches a maximum for the steepest band bending, where the difference between the Fermi level and the band of the graphene channel is greatest, corresponding to $V_G = -40$ V. This explains why the maximum

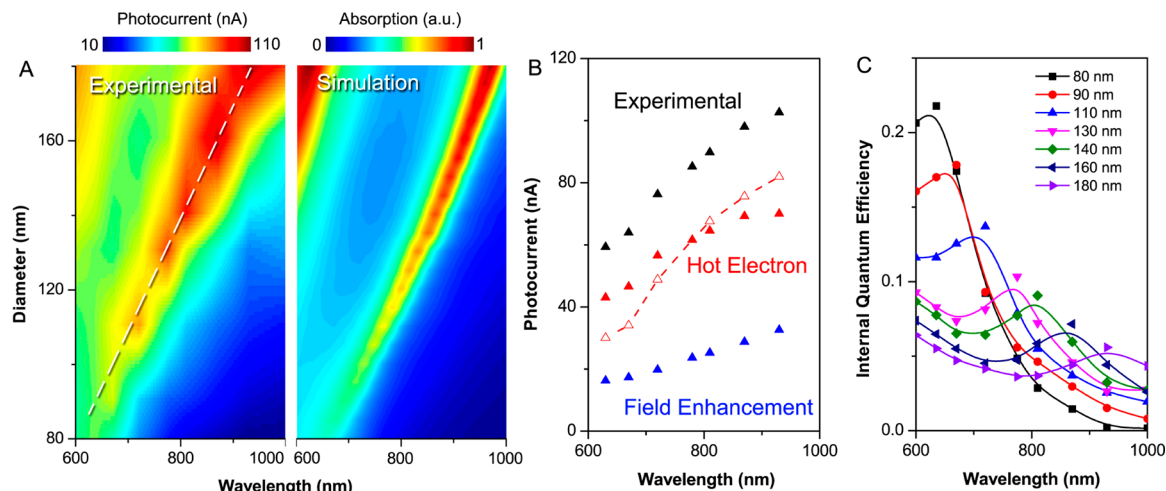


Figure 3. Selective plasmon enhanced graphene photocurrent detection. (A) Left: Graphene photocurrent of different-sized (interpolated) heptamer antenna-patterned sandwich devices for a range of wavelengths extracted from photocurrent line scans, the incident laser power of $10 \mu\text{W}$. Right: Corresponding theoretical absorption spectra $S_{\text{ABS}}(\lambda)$, obtained using FDTD. (B) Measured photocurrent $I^{\text{EXP}}(\lambda)$ (black triangles) and calculated DE photocurrent $I^{\text{DE}}(\lambda)$ (blue triangles). The solid red triangles correspond to the estimated HE photocurrent contribution $E^{\text{HE}}(\lambda) = I^{\text{EXP}}(\lambda) - I^{\text{DE}}(\lambda)$ and the hollow red triangles correspond to the calculated $I^{\text{HE}}(\lambda)$, assuming a wavelength independent C_{HE} with a value corresponding to the 785 nm data. (C) Internal quantum efficiencies of different-sized heptamer antenna-patterned graphene sandwich devices.

photocurrent is always obtained at the positions near the source or drain electrodes, and why position moves closer to the electrodes for larger negative bias voltages. For positive bias voltages, the Fermi level of the graphene channel increases and the band bending becomes less pronounced. For $V_G = +20 \text{ V}$, the band is flat and the photocurrent is negligible. For higher positive bias voltages, the band starts to bend in the opposite direction, and the photocurrent flows in the opposite direction. Similar to the negative bias voltage case, as the positive bias increases, the internal electric field becomes larger, resulting in a corresponding increased photocurrent. Because a gate voltage of nominally $V_G = +20 \text{ V}$ is required to overcome the band bending and establish a flat band condition, the photocurrent observed for $+40 \text{ V}$ is lower than that observed for -40 V bias, as shown in Figure 2C.

The wavelength sensitivity of this device is controlled by the resonant frequency of the antennas: this was demonstrated by varying the size of the heptamer antennas in the device from 80 to 180 nm diameter disks, corresponding to a shift in the heptamer Fano resonance from 650 to 950 nm. Each device was illuminated at nine different wavelengths from 650 to 950 nm, and the wavelength dependent photocurrent responses were measured. By plotting the photocurrent maxima versus the excitation wavelength, we generate a photocurrent spectrum (Figure 3A). The experimental photocurrent spectra display excellent agreement with the absorption spectra calculated using the finite-difference time-domain (FDTD) method, indicating that the photocurrent originates directly from plasmon excitation of the antennas. In our FDTD simulations, we exactly simulated the experimental conditions, including light reflection at the Si/SiO₂ interface.

While the HE contribution to the photocurrent cannot be calculated explicitly due to insufficient knowledge of the potential barrier at the gold graphene interface, the DE contribution can be calculated from FDTD simulations of the plasmon-induced electric near-field enhancements in the graphene structures surrounding the antenna. According to Fermi's golden rule, the local DE carrier generation is proportional to the intensity of the local electric field (E^2).

Therefore, the detected photocurrent can be written as the integrated local field intensity in the graphene surrounding the plasmonic antenna, $I^{\text{DE}} = C_{\text{DE}}(\lambda) / E^2(r) dV$. Here $C_{\text{DE}}(\lambda)$ is a proportionality coefficient containing matrix element and density of states information that we assume to be independent of the electric field intensity and to be an intrinsic property of graphene. The coefficient $C_{\text{DE}}(\lambda)$ can be determined from the experimentally measured photocurrent (10 nA) for the pristine double layered graphene area shown in Figure 2A, by integrating the electric field intensity in the graphene for the incident laser beam area. The result for the DE contribution to the photocurrent is shown by the blue curve in Figure 3B. The plasmonic enhancement of the antennas increase the DE carrier generation significantly, by a factor of 7 compared to the pristine graphene device (Supporting Information). While it is possible that the strain induced in the top graphene layer as it curves around the plasmonic structure may locally increase the coefficient $C_{\text{DE}}(\lambda)$, it is unlikely that this effect will strongly increase the DE contribution to the photocurrent.

The experimental curve in Figure 3B shows that the photocurrent increases with increasing heptamer size (represented by their plasmon resonance wavelengths). A large photoresponsivity $\sim 13 \text{ mA W}^{-1}$ is obtained. While it is clear that the plasmonic DE carrier generation makes an important contribution to the photocurrent, it is obvious that HE carrier generation also contributes significantly. For bare graphene, the photocurrent generated by direct light absorption is the intrinsic photoresponse,¹⁰ however, when the plasmonic antennas are illuminated, the hot electrons generated by decay of the surface plasmons can directly contribute the graphene photocurrent.

By subtracting the calculated DE contribution from the measured photocurrent, we get an estimate for the HE contribution to the photocurrent, $E^{\text{HE}}(\lambda) = I^{\text{EXP}}(\lambda) - I^{\text{DE}}(\lambda)$ (Figure 3B, solid red triangle). HE production in a plasmonic nanoparticle is proportional to the optical absorption $S_{\text{ABS}}(\lambda)$. The resulting hot electron distribution spans the energy interval $[\varepsilon_F, \varepsilon_F + \hbar\omega]$ where ε_F is the Fermi level of Au. While not all hot electrons will transfer into the graphene, the overall HE

contribution to the photocurrent should be proportional to the absorption cross section $I^{\text{HE}} = C_{\text{HE}}(\lambda)S_{\text{ABS}}(\lambda)$. Here the proportionality constant $C_{\text{HE}}(\lambda)$ is expected to depend on the wavelength of incident light, because the electron transmission coefficient across a gold–graphene interface is expected to be energy dependent, and decrease with increasing wavelength. If we assume that C_{HE} is constant and determine its value from the requirement that I^{HE} (785 nm) = E^{HE} (785 nm), the calculated $I^{\text{HE}}(\lambda)$ (Figure 3B, hollow red triangle curve) follows the estimated HE contribution quite well although with a larger slope. Such a discrepancy is not surprising due to our neglect of the energy dependence of the transmission coefficient. For increasing heptamer size, the HE contribution to the photocurrent tends to saturate and the DE contribution plays a larger role. This is expected because the contribution of absorption relative to scattering decreases with increasing nanoparticle size.³⁴ The estimated C_{HE} corresponds to a hot electron current arising from 113% of the initially created hot electron–hole pairs during plasmon decay. This carrier multiplication is due to electron scattering, where an initially created hot electron loses energy by exciting another hot electron in an Auger-like process.³⁵ Because of the unique band structure of graphene, these lower energy electrons can also transfer into the conduction band. Further calculations show that the ratio of $I^{\text{DE}}/I^{\text{HE}}$ remains at nominally 0.5 when the gate voltage is changed from −40 to +40 V (Supporting Information Figure S6).

The internal quantum efficiency (IQE) of the device, that is, the number of carriers produced per incident photon, can be calculated straightforwardly from the measured photocurrent (Supporting Information Text S1) and the incident photon flux on an antenna. The calculated IQE for the different heptamer antenna sizes used in these devices is shown in Figure 3C. A maximum IQE of 22% is obtained for a heptamer sandwich device with a disk diameter of 80 nm (resonance at 630 nm wavelength). At this short wavelength, the dominant contribution to the photocurrent is hot electron generation. For larger heptamers, the IQE decreases but remains at nominally 5–10% over most of the near-infrared range. It is quite likely that the IQE of this type of device can be optimized further with the use of different antenna geometries and additional graphene layers in the device design.

In conclusion, we have developed a very efficient graphene-based light-harvesting device by sandwiching plasmonic nanoantennas between two single layer graphene sheets. The photocurrent is generated by plasmon-enhanced direct carrier excitation of graphene electrons and by plasmon-induced hot electron transfer from the antenna into the surrounding graphene. The spectral sensitivity of the device can be tuned by changing the geometry of the plasmonic antenna, which tunes its Fano resonance. The internal quantum efficiency for the device is ranges between 5 to 20% across the near-infrared to the visible regime. Additionally, the photocurrent can be controlled by applying a gate bias, achieving active device tuning and switching. Combining graphene with antennas extends the optical sensitivity of graphene into new spectral regions inaccessible to the pristine material, and following this lead, may be useful for a variety of future practical device applications.

■ ASSOCIATED CONTENT

■ Supporting Information

Additional information and figures. This material is available free of charge via the Internet at <http://pubs.acs.org>.

■ AUTHOR INFORMATION

Corresponding Author

*E-mail: (Z.F.) zf4@rice.edu; (N.J.H.) halas@rice.edu.

Author Contributions

[†]Equal contributions.

Notes

The authors declare no competing financial interest.

■ ACKNOWLEDGMENTS

We acknowledge Surbhi Lal, Jun Lou, Alexander Urban, and Mark Knight for their helpful discussions; and Lulu Ma and Mingjie Wang for their material preparation. Z.F., Y.W., P.N., and N.J.H. are supported by the Robert A. Welch Foundation (C-1220 and C-1222), the Office of Naval Research (N00014-10-1-0989), and the DoD NSSEFF (N00244-09-1-0067); P.M.A and Z.L. are supported by the Office of Naval Research through the MURI program on graphene.

■ REFERENCES

- (1) Novoselov, K. S.; Geim, A. K.; Morozov, S. V.; Jiang, D.; Zhang, Y.; Dubonos, S. V.; Grigorieva, I. V.; Firsov, A. A. *Science* **2004**, *306*, 666–669.
- (2) Vakil, A.; Engheta, N. *Science* **2011**, *332*, 1291–1294.
- (3) Zhang, Y.; Tang, T.-T.; Girit, C.; Hao, Z.; Martin, M. C.; Zettl, A.; Crommie, M. F.; Shen, Y. R.; Wang, F. *Nature* **2009**, *459*, 820–823.
- (4) Li, X.; Zhu, Y.; Cai, W.; Borysiak, M.; Han, B.; Chen, D.; Piner, R. D.; Colombo, L.; Ruoff, R. S. *Nano Lett.* **2009**, *9*, 4359–4363.
- (5) Wang, X.; Zhi, L.; Mullen, K. *Nano Lett.* **2007**, *8*, 323–327.
- (6) Xia, F.; Mueller, T.; Lin, Y.-m.; Valdes-Garcia, A.; Avouris, P. *Nat. Nanotechnol.* **2009**, *4*, 839–843.
- (7) Ju, L.; Geng, B.; Horng, J.; Girit, C.; Martin, M.; Hao, Z.; Bechtel, H. A.; Liang, X.; Zettl, A.; Shen, Y. R.; Wang, F. *Nat. Nanotechnol.* **2011**, *6*, 630–634.
- (8) Lemme, M. C.; Koppens, F. H. L.; Falk, A. L.; Rudner, M. S.; Park, H.; Levitov, L. S.; Marcus, C. M. *Nano Lett.* **2011**, *11*, 4134–4137.
- (9) Song, J. C. W.; Rudner, M. S.; Marcus, C. M.; Levitov, L. S. *Nano Lett.* **2011**, *11*, 4688–4692.
- (10) Gabor, N. M.; Song, J. C. W.; Ma, Q.; Nair, N. L.; Taychatanapat, T.; Watanabe, K.; Taniguchi, T.; Levitov, L. S.; Jarillo-Herrero, P. *Science* **2011**, *334*, 648–652.
- (11) Bonaccorso, F.; Sun, Z.; Hasan, T.; Ferrari, A. C. *Nat. Photonics* **2010**, *4*, 611–622.
- (12) Moskovits, M. *Rev. Mod. Phys.* **1985**, *57*, 783–826.
- (13) Barnes, W. L.; Dereux, A.; Ebbesen, T. W. *Nature* **2003**, *424*, 824–830.
- (14) Halas, N. J.; Lal, S.; Chang, W. S.; Link, S.; Nordlander, P. *Chem Rev* **2011**, *111*, 3913–3961.
- (15) Atwater, H. A.; Polman, A. *Nat. Mater.* **2010**, *9*, 205–213.
- (16) Polman, A. *Science* **2008**, *322*, 868–869.
- (17) Walters, R. J.; van Loon, R. V. A.; Brunets, I.; Schmitz, J.; Polman, A. *Nat. Mater.* **2010**, *9*, 21–25.
- (18) Yu, N.; Wang, Q. J.; Kats, M. A.; Fan, J. A.; Khanna, S. P.; Li, L.; Davies, A. G.; Linfield, E. H.; Capasso, F. *Nat. Mater.* **2010**, *9*, 730–735.
- (19) Pacifici, D.; Lezec, H. J.; Atwater, H. A. *Nat. Photonics* **2007**, *1*, 402–406.
- (20) Giessen, H.; Lippitz, M. *Science* **2010**, *329*, 910–911.

- (21) Echtermeyer, T. J.; Britnell, L.; Jasnos, P. K.; Lombardo, A.; Gorbachev, R. V.; Grigorenko, A. N.; Geim, A. K.; Ferrari, A. C.; Novoselov, K. S. *Nat. Commun.* **2011**, *2*, 458.
- (22) Liu, Y.; Cheng, R.; Liao, L.; Zhou, H. L.; Bai, J. W.; Liu, G.; Liu, L. X.; Huang, Y.; Duan, X. F. *Nat. Commun.* **2011**, *2*.
- (23) Schedin, F.; Lidorikis, E.; Lombardo, A.; Kravets, V. G.; Geim, A. K.; Grigorenko, A. N.; Novoselov, K. S.; Ferrari, A. C. *ACS Nano* **2010**, *4*, 5617–5626.
- (24) Koppens, F. H. L.; Chang, D. E.; de Abajo, F. J. G. *Nano Lett.* **2011**, *11*, 3370–3377.
- (25) Fan, J. A.; Wu, C. H.; Bao, K.; Bao, J. M.; Bardhan, R.; Halas, N. J.; Manoharan, V. N.; Nordlander, P.; Shvets, G.; Capasso, F. *Science* **2010**, *328*, 1135–1138.
- (26) Luk'yanchuk, B.; Zheludev, N. I.; Maier, S. A.; Halas, N. J.; Nordlander, P.; Giessen, H.; Chong, C. T. *Nat. Mater.* **2010**, *9*, 707–715.
- (27) Stockman, M. I. *Nature* **2010**, *467*, 541–542.
- (28) Shalaev, V. M.; Douketis, C.; Stuckless, J. T.; Moskovits, M. *Phys. Rev. B* **1996**, *53*, 11388–11402.
- (29) Mubeen, S.; Hernandez-Sosa, G.; Moses, D.; Lee, J.; Moskovits, M. *Nano Lett.* **2011**, *11*, 5548–5552.
- (30) Knight, M. W.; Sobhani, H.; Nordlander, P.; Halas, N. J. *Science* **2011**, *332*, 702–704.
- (31) Li, X.; Cai, W.; An, J.; Kim, S.; Nah, J.; Yang, D.; Piner, R.; Velamakanni, A.; Jung, I.; Tutuc, E.; Banerjee, S. K.; Colombo, L.; Ruoff, R. S. *Science* **2009**, *324*, 1312–1314.
- (32) Schwierz, F. *Nat. Nanotechnol.* **2010**, *5*, 487–496.
- (33) Giovannetti, G.; Khomyakov, P. A.; Brocks, G.; Karpan, V. M.; van den Brink, J.; Kelly, P. J. *Phys. Rev. Lett.* **2008**, *101*, 026803.
- (34) Hulst, H. C. v. d. *Light scattering by small particles*; Dover Publications: New York, 1981; p 470.
- (35) Frischkorn, C.; Wolf, M. *Chem. Rev.* **2006**, *106*, 4207–4233.